Influence of local tensile direction on martensitic variant selection in the superelastic Ti-20Zr-12Nb-2Sn alloy

J. J. Gao, Y. Q. Zhao, F. X. Yin, P. Castany, T. Gloriant

Materials Science & Engineering A 955 (2026) 149864

Contents lists available at ScienceDirect

Materials Science & Engineering A

journal homepage: www.elsevier.com/locate/msea

Influence of local tensile direction on martensitic variant selection in the superelastic Ti-20Zr-12Nb-2Sn alloy

J.J. Gao [a,b,*], Y.Q. Zhao [c], F.X. Yin [d], P. Castany [b,**], T. Gloriant [b]

[a] School of Materials Science and Engineering, Tianjin University of Technology, Tianjin, 300384, China
[b] Univ Rennes, INSA Rennes, CNRS, ISCR UMR 6226, 35000, Rennes, France
[c] Northwest Institute for Nonferrous Metal Research, Xi' an, 710016, China
[d] School of Materials Science and Engineering, Hebei University of Technology, Tianjin, 300132, China

ARTICLE INFO

Keywords:
Titanium alloys
Ti-Zr-Nb-Sn
Superelasticity
Stress-induced martensitic transformation
Martensitic variant

ABSTRACT

The superelastic Ti-20Zr-12Nb-2Sn (at.%) alloy after solution treatment at 700 °C for 30 min was investigated by cyclic tensile tests, *in situ* synchrotron X-ray diffraction (SXRD), and electron back-scattered diffraction (EBSD) after plastic deformation. The reversible stress-induced martensitic (SIM) α" transformation was validated by *in situ* SXRD during loading/unloading, and the crystallographic orientation relationship between β phase and SIM α" phase was investigated by EBSD from two specimens after 3 % and 7 % of deformation. In particular, martensitic variant selection is governed by the local tensile direction for individual grains. The maximum transformation strain varies with local tensile directions, but the selected martensitic variant consistently corresponds to the one exhibiting the highest transformation strain when the local tensile direction is near $<101>_\beta$ or $<111>_\beta$ directions. However, the activated variant deviates from this rule when the tensile direction is near $<100>_\beta$. This comprehensive study of the unexpected deviation in martensitic variant selection as a function of local tensile direction provides a better understanding of the superelastic performance of Ti-based alloys.

1. Introduction

Titanium based alloys are extensively manufactured as biomedical devices, such as stents, orthopedic staples, guide wires … owing to their superelasticity and shape memory effect [1]. At present, the near-equimolar NiTi alloys are the most widely used ones for clinical applications. Nevertheless, the high-content Ni addition in NiTi alloys could lead to cytotoxicity and hypersensitivity in the human body [2]. The metastable β-Ti alloys composed of biocompatible elements, such as Zr, Nb, Mo, Ta, Sn, have then been developed to replace NiTi alloys [3–10]. Ti-Nb based alloys draw great attention attributed to their low elastic modulus, high strength and superelastic/shape memory effect. For example, the well-known Ti-24Nb-4Zr-8Sn (wt%) alloy (Ti2448 for short) shows 990 MPa ultimate tensile strength, 58 GPa Young's modulus, and 2.7 % recovery strain [9], as well as superior biocompatibility [10]. However, the superelastic performance of the reported Ti-Nb based alloys is much lower than NiTi alloys. The high-performance biomedical superelastic titanium alloys are thus urgent to be developed [11]. In recent years, Miyazaki et al. proposed novel Ti-Zr-Nb-Sn type superelastic alloys, and reported that the Ti-24Zr-10Nb-2Sn (at.%) alloy exhibited recovery strain of 7 %, which is owing to the improved transformation strain through higher Zr addition and favorable $\{001\}<110>_\beta$ recrystallization texture [12]. In addition, these Ti-Zr-Nb-Sn type alloys also presented excellent biocompatibility [13]. Therefore, considerable Ti-Zr-(Hf) based [14–21], as well as Ti-Hf based [22] superelastic alloys have been designed and fabricated.

As is well known, the superelasticity in metastable β-Ti alloys, whether for Ti-Nb based or Ti-Zr based alloys, is due to the reversible transition between the parent β phase (body-centered cubic) and the SIM α" phase (C-centered orthorhombic) during stress loading and unloading. The related transformation strain can be then estimated with cell parameters of the two phases [23–28]. For one crystallographic orientation of β phase, six correspondence variants (CV) with different transformation strains can be formed. When a stress is applied, a variant selection occurs and promotes the formation of the CV with the highest transformation strain value [29–32]. However, the measured recovery strain values are less than the corresponding calculated ones for polycrystalline materials. For instance, the recovery strain is only 3.5 % for

* Corresponding author. School of Materials Science and Engineering, Tianjin University of Technology, Tianjin, 300384, China.
** Corresponding author.
E-mail addresses: Jingjun_gao@email.tjut.edu.cn (J.J. Gao), philippe.castany@insa-rennes.fr (P. Castany).

https://doi.org/10.1016/j.msea.2026.149864
Received 16 December 2025; Received in revised form 23 January 2026; Accepted 29 January 2026
Available online 30 January 2026

the Ti-20Zr-3Mo-3Sn (at.%) alloy with advantageous {001}<101>$_\beta$ recrystallization texture, but the theoretical value is 7.3 % along <101>$_\beta$ crystallographic direction, which is far away from the measured one [33]. The present letter thus attempts to investigate the effect of the local tensile direction in the variant selection process during deformation, with the aim to highlight the role of this phenomenon in the difference between actual and theoretical recoverable strain values. In this study, the superelastic Ti-20Zr-12Nb-2Sn (at.%) alloy was investigated after plastic deformation of 3 % and 7 % by cyclic tensile test, *in situ* SXRD and EBSD. The martensitic variant selection depending on local tensile direction is then comprehensively analyzed for the individual grains and reported for the first time.

2. Materials and methods

The pure materials (99.995 % Ti, 99.95 % Zr, 99.95 % Nb, 99.99 % Sn) were used to obtain the Ti-20Zr-12Nb-2Sn (at.%, Ti20122 for short) ingot by arc melting technique under high-purity Ar atmosphere. Homogenization was conducted on the ingot at 950 °C for 24 h in Ar quartz tube, and then followed by water quenching. This ingot was cold rolled until 90 % reduction and machined into tensile specimens measuring 3 mm in width, 0.5 mm in thickness and with a gage length of 15 mm. Solution treatment at 700 °C for 30 min was applied to the tensile samples, followed by water quenching, and finally cleaned in acid solution (50 % HF + 50 % HNO_3, vol%) to remove oxidation layer.

The superelastic performance of the alloy was evaluated by cyclic tensile tests under the strain rate of 2×10^{-4} s^{-1} with extensometer. Each increasing step of strain was set as 0.5 % during loading and followed by a total stress releasing during unloading before 5 % of strain (with the same strain rate). Then, the increasement was 1 % until 7 % of strain. The 3 % and 7 % samples were prepared for EBSD characterization from two interrupted cyclic tensile tests.

Electro-polishing method was used to prepare EBSD samples (0 %, 3 % and 7 % of strain) with a 10 % perchloric acid and 90 % methanol (vol %) solution at −40 °C and 20 V after mechanical polishing. EBSD experiment was conducted on a Zeiss scanning electron microscope (SEM) equipped with Oxford Symmetry S3 detector under the acceleration voltage of 20 kV. EBSD data was finally analyzed by AztecCrystal software.

In situ synchrotron X-ray diffraction (SXRD) experiment during cyclic tensile tests was conducted at the ID-22 beamline of the European Synchrotron Radiation Facility (ESRF, Grenoble, France) with a high-energy incident X-ray beam (λ = 0.35453630 Å). The strain rate is 2×10^{-4} s^{-1} and deformation steps are the same as the aforementioned cyclic tensile tests. Diffractograms were acquired through a nine-channel detector over the 2θ angular range 6°–20°. The acquisition steps are indicated by the blue spots on the tensile curve in Fig. 1a.

3. Results and discussion

Fig. 1a is the engineering stress-strain curve from cyclic tensile tests for the thermal treated Ti20122 alloy at 700 °C for 30 min. The superelastic performance is confirmed from the hysteresis between loading/unloading [34–36] and the maximum recovery strain is estimated as 3.1 %. Fig. 1b shows the inverse pole figure from EBSD experiment for the undeformed specimen, and a {111}<101>$_\beta$ recrystallized texture can be identified. While the pole density is rather high in the normal direction (more than 4), the rolling/tensile direction is not strongly preferentially aligned along <101> (with a pole density lower than 2). This will allow a variety of grain orientations to be analyzed after deformation. Furthermore, the partial *in situ* SXRD profiles, as shown in Fig. 1c–d, validate the occurrence of the reversible martensitic transformation between parent β phase and SIM α" phase during cyclic tensile tests [28,33]. From this result, it is apparent that the $(110)_\beta$ peak decreases with increasing strain, while the typical martensitic peaks of $(020)_{\alpha''}$, $(002)_{\alpha''}$, $(021)_{\alpha''}$, $(111)_{\alpha''}$ increase. The cell parameters are measured as $a_\beta = 0.3360$ nm, $a_{\alpha''} = 0.3187$ nm, $b_{\alpha''} = 0.5043$ nm, $c_{\alpha''} = 0.4787$ nm.

Fig. 2 shows full EBSD results of Euler angle maps (Fig. 2a–c) and phase maps (Fig. 2b–d) from Ti20122 alloy for the two strained

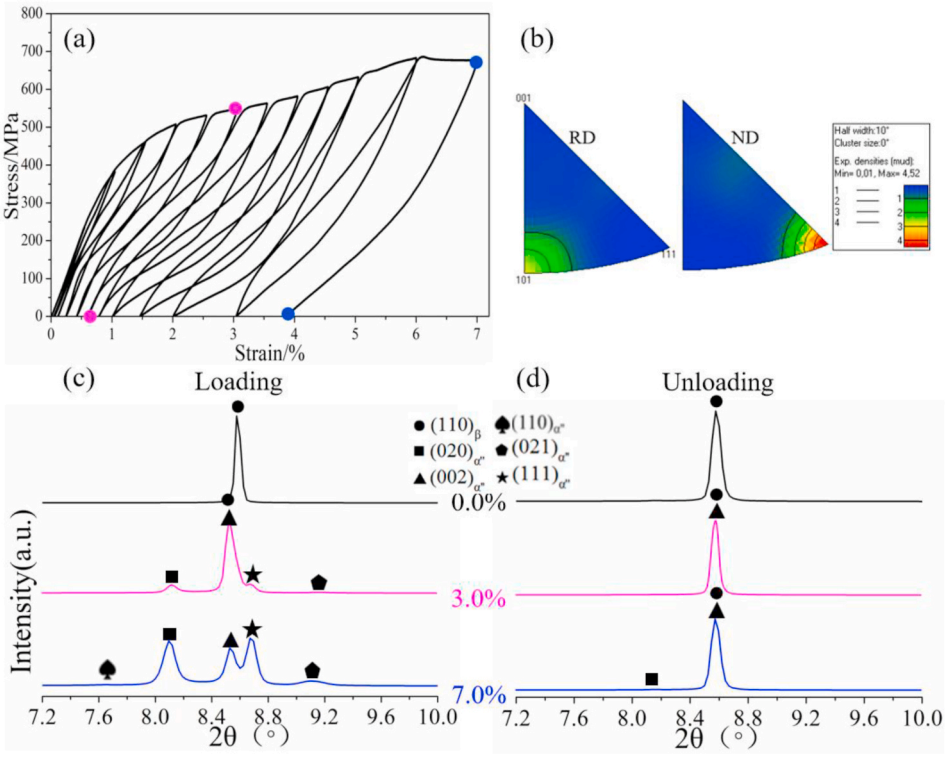

Fig. 1. Cyclic engineering tensile curve of the Ti20122 alloy (a), the corresponding EBSD inverse pole figure before deformation (b), *in situ* SXRD profiles during loading (c) and unloading (d) acquired from the specimens strained to 0 %, 3 % and 7 %.

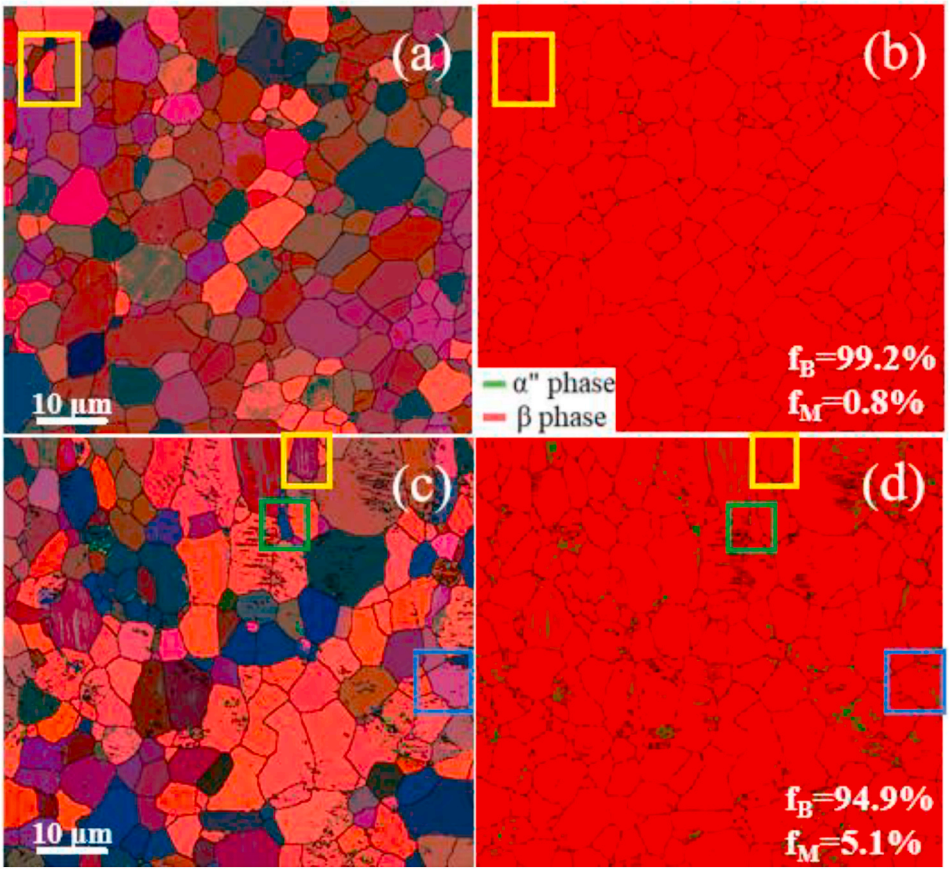

Fig. 2. The EBSD Euler angle maps (a,c) and the corresponding phase maps (b,d) from specimens strained to 3 % (a–b) and 7 % (c–d) for the Ti20122 alloy.

specimens: the first one is unloaded from 3 % of strain (Fig. 2a–b), and the second one is unloaded from 7 % of strain (Fig. 2c–d). Before deformation, the alloy is full of β phase, which is validated with the *in situ* SXRD profile. After plastic deformation, both β phase and needle-like SIM α" phase are indexed by EBSD. With the strain increasing from 3 % to 7 %, the surface fraction of β phase decreases from 99.2 % to 94.9 %, and the surface fraction of SIM α" phase in turn increases from 0.8 % to 5.1 %. The low value of the surface fraction of martensite is consistent with the superelastic behavior of this alloy shown from SXRD data. The main part of SIM α" is indeed reverted back to β phase after removing the

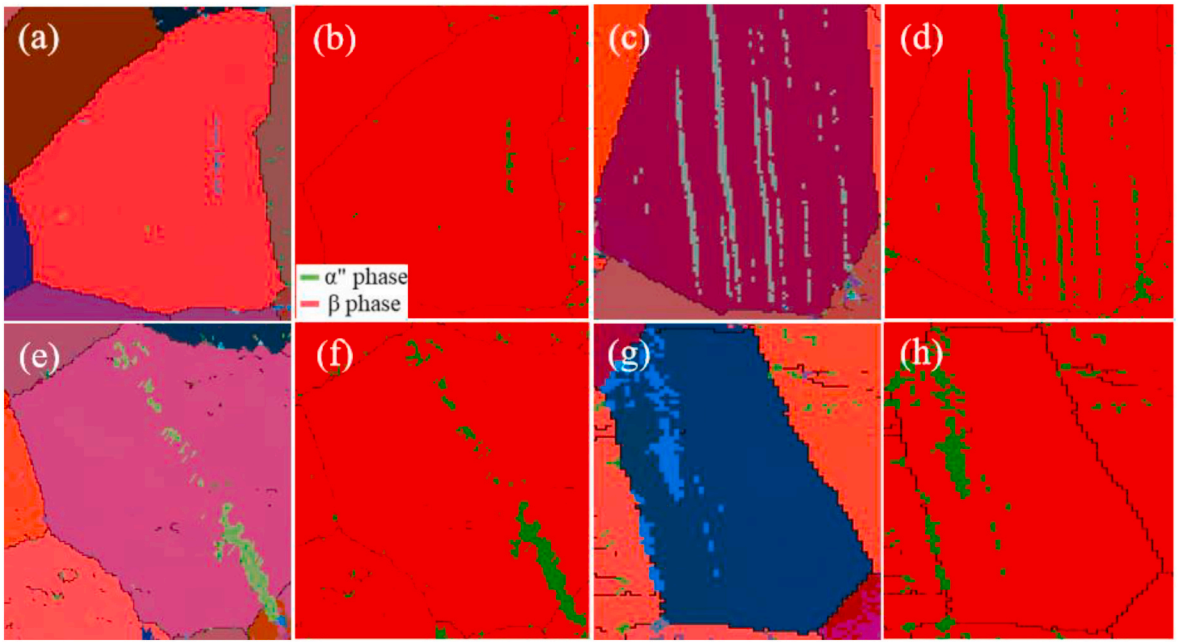

Fig. 3. The EBSD Euler angle maps (a,c,e,g) and phase maps (b,d,f,h) for β and SIM α" phases of the enlarged rectangle areas in Fig. 2.

stress, and the observed residual α" martensite is a minor part that is retained due to the onset of plastic deformation. This residual α" martensite will then be used as a signature of the SIM α" to characterize its features. Therefore, this EBSD study is regarded as a subset of the stress-induced martensite population, rather than as a one-to-one correspondence between residual martensitic variants and the macroscopic superelasticity. Although the SIM is fully reversible in most grains, those with residual martensite allow to reveal the effect of local tensile direction on selected martensitic variants and the tendency of variant selection.

In order to investigate the relationship between local tensile direction and martensitic variant selection, the representative grains with residual SIM α" needles are shown in Fig. 3. Fig. 3a,c,e,g and Fig. 3b,d,f,h are respectively the zoomed areas in Euler angle maps and phase maps, which are captured from the areas delimited by rectangles in Fig. 2, for both parent β phase and SIM α" phase. Compared with the 3 % strained sample (Fig. 3a–b), the residual SIM α" plates are much more significant with the stain increasing to 7 % (Fig. 3c–h). In addition, it is worth to notice that the martensitic α" plates only display a single orientation in each grain. This observation is also validated by the other 17 grains in the supplementary materials (Sup.1 to Sup.17), which are taken from Fig. 2c. The detailed orientation relationship between β phase and SIM α" phase are then further examined by stereographic projection in Fig. 4 hereafter.

Fig. 4 is the stereographic projection of parent β phase (Fig. 4a–c,e,g) and SIM α" phase (Fig. 4b–d,f,h) for the strained 3 % (Fig. 3a–b) and 7 % (Fig. 3c–h) specimens from Fig. 3a,c,e,g, respectively. For a better readability, only the three $\{001\}_{\beta/\alpha''}$ planes as well as the most related poles and traces of interest are displayed in the stereographic projections, where solid circles indicate poles of crystallographic planes and open circles mean crystallographic directions. For the 3 % strained sample (Fig. 4a–b), the β phase and SIM α" phase clearly follows the $[100]_{\alpha''}\|[001]_{\beta}$ and $[101]_{\alpha''}\|<111>_{\beta}$ conventional orientation relationships [26,30,37], and the correspondence variant 6 (namely CV6) is activated. Hence, there is no twinning formation during loading/unloading. For this CV6, both $(-5,5,7)_{\beta}$ and $(5,-5,7)_{\beta}$ habit plane variants can be equally triggered, but only the $(-5,5,7)_{\beta}$ variant is consistent with the EBSD result (Fig. 3b). According to the tensile direction $[12,-7,-2]_{\beta}$, the transformation strain for the six CV is then calculated with the equation of $\varepsilon_i = \mathbf{T}^{\mathbf{t}}\cdot\varepsilon^{(i)}\cdot\mathbf{T}$, where $\boldsymbol{T}$ is tensile direction, $\varepsilon^{(i)}$ is lattice deformation matrix, ε_i is transformation strain for the ith CV, and the result is shown in Table 1 (the 2nd column). One can notice that the CV6 offers the highest transformation strain of 5.56 %, which corresponds well with the analysis of stereographic projections (Fig. 4a–b). This method is also applied to the 7 % sample, and the stereographic projections as well as the calculated transformation strains are respectively shown in Fig. 4c-h and Table 1 (the 3rd column to the 5th column). For the grain in Fig. 3c, the selected martensitic variant is CV6, and it indeed provides the maximum transformation strain (5.91 %), which is the same as the 3 % strained sample (Fig. 4b). Even though the selected martensitic variant CV5 has the highest transformation strain of 2.71 % in Fig. 3e, this value significantly decreases from 5.91 % to 2.71 % in comparison to the previous case. This is due to the local tensile direction variation from $[-8,6,1]_{\beta}$ to $[15,15,-14]_{\beta}$, which is close to $<111>_{\beta}$ direction. What the most noticeable is that the observed martensitic variant by EBSD is CV3 in Fig. 3g, while this variant is on compression state (−4.23 %, the 5th column in Table 1).

In order to further highlight the influence of local tensile direction on martensitic variant selection, another 17 grains are carefully studied in the supplementary materials (Sup.1 to Sup.17, and Sup-Table 1). From Grain 1 to Grain 15, the real activated martensitic variant is the one with the highest transformation strain, and their tensile directions are near $<101>_{\beta}$. However, the actual martensitic variants do not have the highest transformation strains in Grain 16 (3.40 %, CV6) and Grain 17 (3.00 %, CV3), and these values obviously are much lower than the aforementioned 15 grains due to their near $<100>_{\beta}$ local tensile direction. The mechanism at the origin of this deviation is however not evident. Dislocation slip activity in the β phase could affect the variant

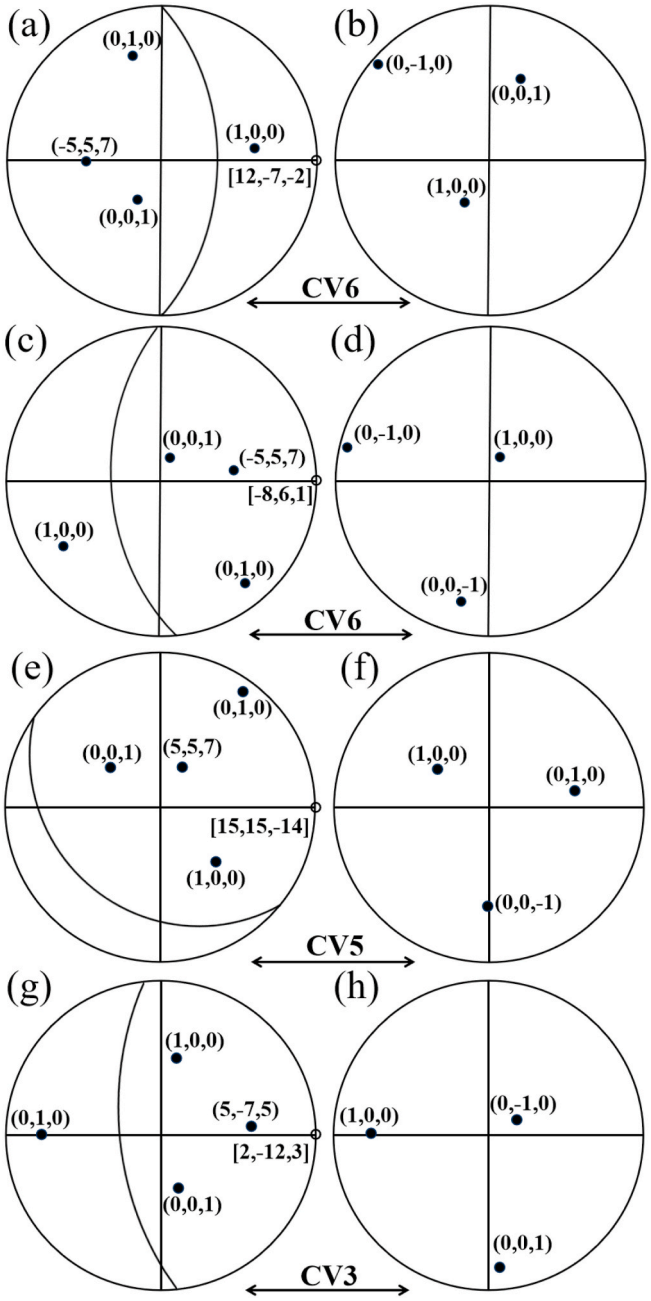

Fig. 4. Stereographic projections of the detected β phase (a,c,e,g) and SIM α" phase (b,d,f,h) for the strained 3 % (a–b) and 7 % (c–h) specimens from Fig. 3a, c, 3e, and 3g, respectively.

Table 1
The calculated transformation strains for each α" martensitic correspondence variant.

Variants	3 % of strain (Fig. 4b)	7 % of strain (Fig. 4d)	7 % of strain (Fig. 4f)	7 % of strain (Fig. 4h)
CV1	−2.46 %	−1.68 %	−1.31 %	1.98 %
CV2	−3.22 %	−2.32 %	2.20 %	4.45 %
CV3	0.64 %	−0.05 %	−1.31 %	**−4.23 %**
CV4	1.96 %	−0.80 %	2.20 %	−4.64 %
CV5	0.96 %	0.79 %	**2.71 %**	2.12 %
CV6	**5.56 %**	**5.91 %**	−1.05 %	3.77 %

selection of martensite by acting as nucleation sites. However, the SXRD data (Fig. 1c) shows that the β phase is totally transformed into martensite for a strain of 7 %, as the peak of β phase cannot be detected, meaning that martensite is already formed when the dislocation activity became the most significant. Another hypothesis is that the resolved shear stress is higher for CV with lower transformation strain values than for CV with the highest transformation strain value. However, a previous study demonstrated that the Schmid factor and transformation strain calculations lead to the same hierarchy of CV [38]. Therefore, resolved shear stress follows the same trend as transformation strain and cannot explain the observed deviation. From the present experiments, the local deviation of the tensile direction resulting from incompatibility interactions of neighboring grains seems the most probable cause of the observed deviation in the variant selection of martensite. However, further research is required to validate this hypothesis and deeply understand the underlying physical or crystallographic mechanism.

Fig. 5 is a $[100]_\beta$ stereographic projection summarizing the distribution of tensile directions for all the investigated 21 grains in this study. It is noticeable that when the local tensile direction is near $<101>_\beta$ (81.0 %) or $<111>_\beta$ (4.7 %), the selected martensitic variant is the one with the maximum transformation strain. However, the activated variants are not the ones with the highest transformation strain when the tensile direction is around $<100>_\beta$ directions (14.3 %). This investigation highlights an unexpected explanation of the decrease of the measured recoverable strain that can occur in superelastic Ti-based alloys. In addition to the natural decrease of the theoretical transformation strain when the tensile direction deviates from $<101>_\beta$, the activated CV can be not the one with the highest transformation strain, leading to a worsening of the decrease in the recoverable strain. This phenomenon was never reported in metastable β titanium alloys before and strengthens the need to favor a texture with $<101>_\beta$ directions that are closely aligned with the tensile direction.

4. Conclusion

In summary, the microstructure of Ti20122 alloy thermal treated at 700 °C for 30 min was investigated by cyclic tensile tests, *in situ* SXRD and EBSD after plastic deformation. The reversible SIM α" transformation is confirmed through *in situ* SXRD experiment at 3 % and 7 % of strain during loading/unloading. Both β phase and residual SIM α" phase were determined, and their crystallographic orientation relationship was analyzed by EBSD. All the SIM α" phase followed the conventional orientation relationship with parent β phase, and no twinning systems were detected. In particular, martensitic variant selection and transformation strain are influenced by the local tensile direction. When this direction is near $<101>_\beta$ or $<111>_\beta$, the selected martensitic variant is the one which displays the highest transformation strain, as expected. But when the local tensile direction is near the $<100>_\beta$ direction, the activated variant is not the one with the maximum transformation strain, and even can be on compression state, which has not been reported before in superelastic titanium alloys. This comprehensive study about martensitic variant selection as a function of local tensile direction gives a better understanding of superelastic performance in Ti-based alloys.

CRediT authorship contribution statement

J.J. Gao: Writing – review & editing, Writing – original draft, Methodology, Investigation, Formal analysis, Data curation, Conceptualization. **Y.Q. Zhao:** Writing – review & editing, Formal analysis. **F.X. Yin:** Writing – review & editing, Formal analysis. **P. Castany:** Writing – review & editing, Visualization, Validation. **T. Gloriant:** Writing – review & editing, Visualization, Validation.

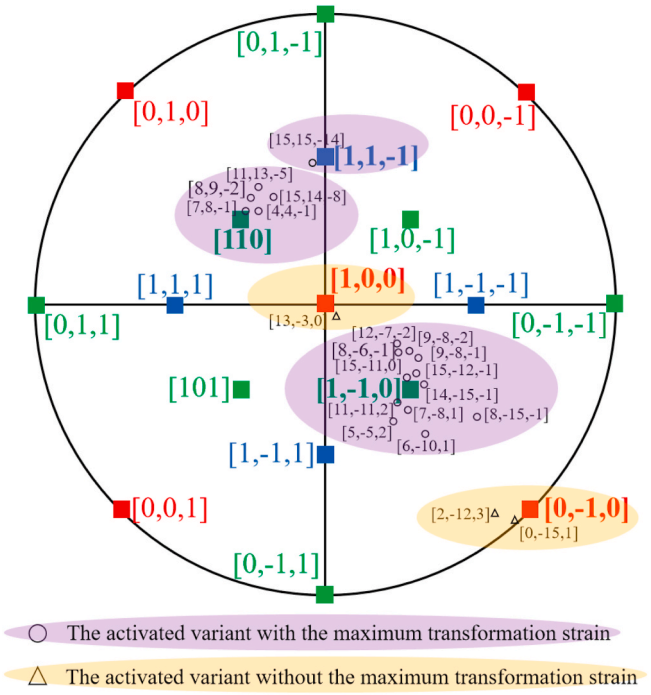

Fig. 5. $[100]_\beta$ stereographic projection to indicate the local tensile direction distribution for the 21 investigated grains.

Originality statement

I write on behalf of myself and all co-authors to confirm that the results reported in the manuscript are original and neither the entire work, nor any of its parts have been previously published. The authors confirm that the article has not been submitted to peer review, nor has been accepted for publishing in another journal. The author(s) confirms that the research in their work is original, and that all the data given in the article are real and authentic. If necessary, the article can be recalled, and errors corrected.

Declaration of competing interest

The authors declare that they have no known competing financial interests or personal relationships that could have appeared to influence the work reported in this paper.

Acknowledgments

This work was financially sponsored by National Natural Science Foundation of China (No.52301305), China Postdoctoral Science Foundation (No.2024M754158), Tianjin Natural Science Foundation (No.23JCQNJC00580), and Heilongjiang Postdoctoral Science Foundation (No.LBH-Z24125). J.J. Gao, P. Castany, T. Gloriant also acknowledge the European Synchrotron Radiation Facility (ESRF) for provision of synchrotron radiation facilities under proposal number MA-3956 and would like to thank beam scientist A.Fitch for assistance and support in using beamline ID22.

Data availability

Data will be made available on request.

References

[1] M. Niinomi, M. Nakai, J. Hieda, Development of new metallic alloys for biomedical applications, Acta Biomater. 8 (2012) 3888–3903.

[2] D.J. Wever, A.G. Veldhuizen, M.M. Sanders, J.M. Schakenraad, J.R. van Horn, Cytotoxic, allergic and genotoxic activity of a nickel-titanium alloy, Biomaterials 18 (1997) 1115–1120.
[3] C. Talbot, N. Church, N. Jones, Observation of α phase nucleation within ω precipitates with novel orientation relationship in a low misfit metastable β-Ti alloy through EBSD, Scripta Mater. 255 (2025) 116335.
[4] M. Qiang, X. Yang, G. Wang, X. Liu, L. Luo, Q. Ren, J. Wang, Enhanced strength and reduced elastic modulus of biomedical metastable β Ti–Nb alloy via intermediate phase transformation, Mater. Des. 251 (2025) 113662.
[5] Y. Gao, J. Chen, Y. Gan, X. Liang, H. Chen, D. Zeng, C. Yang, W. Jiang, C. Ma, W. Xiao, Biomedical Ti–Nb–O alloy with high strength and ultra-low Young's modulus, Mater. Res. Lett. (2025).
[6] X. Luo, T. Song, A. Gebert, K. Neufeld, I. Kaban, H. Ma, W. Cai, H. Lu, D. Li, N. Li, Y. Li, C. Yang, Programming crystallographic orientation in additive-manufactured beta-type titanium alloy, Adv. Sci. 10 (2023) 2302884.
[7] N. Nohira, W.-T. Chiu, M. Tahara, H. Hosoda, Microstructural changes and mechanical property response to aging heat treatment in hypereutectoid Ti–Au–Mo biomedical alloys, Mater. Sci. Eng. A 912 (2024) 146956.
[8] Y. Fu, W. Xiao, D. Kent, J. Rong, X. Zhao, C. Ma, Natural aging of a metastable β-type titanium alloy to simultaneously enhance yield strength and uniform elongation, Scripta Mater. 234 (2023) 115569.
[9] Y. Yang, P. Castany, M. Cornen, I. Thibon, F. Prima, T. Gloriant, Texture investigation of the superelastic Ti–24Nb–4Zr–8Sn alloy, J. Alloys Compd. 591 (2014) 85–90.
[10] X. Li, T. Chen, J. Hu, S. Li, Q. Zou, Y. Li, N. Jiang, H. Li, J. Li, Modified surface morphology of a novel Ti–24Nb–4Zr–7.9Sn titanium alloy via anodic oxidation for enhanced interfacial biocompatibility and osseointegration, Colloids Surf. B Biointerfaces 144 (2016) 265–275.
[11] L. Héraud, P. Castany, M.F. Ijaz, D.-M. Gordin, T. Gloriant, Large-strain functional fatigue properties of superelastic metastable β titanium and NiTi alloys: a comparative study, J. Alloys Compd. 953 (2023) 170170.
[12] L. López Pavón, H.Y. Kim, H. Hosoda, S. Miyazaki, Effect of Nb content and heat treatment temperature on superelastic properties of Ti–24Zr–(8–12) Nb–2Sn alloys, Scripta Mater. 95 (2015) 46–49.
[13] J. Fu, A. Yamamoto, H.Y. Kim, H. Hosoda, S. Miyazaki, Novel Ti-base superelastic alloys with large recovery strain and excellent biocompatibility, Acta Biomater. 17 (2015) 56–67.
[14] J.J. Gao, P. Castany, T. Gloriant, Grain size dependent martensitic twinning behavior in superelastic Ti-20Zr-12Nb-2Sn alloy: a comparative study, Acta Mater. 296 (2025) 121260.
[15] S. Li, M.-S. Choi, T.-H. Nam, Phase stability of the amorphous phase and non-equilibrium phase in a β Ti-Zr-based shape memory alloy, Scripta Mater. 195 (2021) 113721.
[16] M.F. Ijaz, H.Y. Kim, H. Hosoda, S. Miyazaki, Superelastic properties of biomedical (Ti–Zr)–Mo–Sn alloys, Mater. Sci. Eng. C 48 (2015) 11–20.
[17] L. Kong, B. Wang, X. Meng, Z. Gao, Superelasticity by introductions of Cr into the Ti-Zr-Nb-Sn strain glass alloy toward the elastocaloric application, J. Alloys Compd. 935 (2023) 168156.
[18] J.J. Gao, P. Castany, T. Gloriant, Synthesis and characterization of a new TiZrHfNbTaSn high-entropy alloy exhibiting superelastic behavior, Scripta Mater. 198 (2021) 113824.
[19] W. Tasaki, K. Nakano, Y. Sato, T. Koyano, S. Miyazaki, H.Y. Kim, Effects of Zr and Hf on superelasticity, shape memory effect and microstructure of β-type (Ti–Zr–Hf)–Nb–Sn multi-principal element alloys with low magnetic susceptibility, Mater. Sci. Eng. A 908 (2024) 146760.
[20] L. Kong, B. Wang, X. Meng, Z. Gao, Texture evolution, microstructure, and superelastic properties of different cold-rolled Ti-Zr-Nb-Sn strain glass alloys, Mater. Char. 193 (2022) 112309.
[21] J.J. Gao, P. Castany, T. Gloriant, Complex multi-step martensitic twinning process during plastic deformation of the superelastic Ti-20Zr-3Mo-3Sn alloy, Acta Mater. 236 (2022) 118140.
[22] M.F. Ijaz, D. Laillé, L. Héraud, D.-M. Gordin, P. Castany, T. Gloriant, Design of a novel superelastic Ti-23Hf-3Mo-4Sn biomedical alloy combining low modulus, high strength and large recovery strain, Mater. Lett. 177 (2016) 39–41.
[23] T. Yao, K. Du, H. Wang, Z. Huang, C. Li, L. Li, Y. Hao, R. Yang, H. Ye, In situ scanning and transmission electron microscopy investigation on plastic deformation in a metastable β titanium alloy, Acta Mater. 133 (2017) 21–29.
[24] Z.W. Zhu, C.Y. Xiong, J. Wang, R.G. Li, Y. Ren, Y.D. Wang, Y. Li, In situ synchrotron X-ray diffraction investigations of the physical mechanism of ultra-low strain hardening in Ti-30Zr-10Nb alloy, Acta Mater. 154 (2018) 45–55.
[25] S. Guo, Y. Shang, J. Zhang, Q. Meng, X. Cheng, X. Zhao, In situ synchrotron X-ray diffraction study of deformation behaviour of a metastable β-type Ti-33Nb-4Sn alloy, Intermetallics 86 (2017) 20–24.
[26] H.Y. Kim, Y. Ikehara, J.I. Kim, H. Hosoda, S. Miyazaki, Martensitic transformation, shape memory effect and superelasticity of Ti–Nb binary alloys, Acta Mater. 54 (2006) 2419–2429.
[27] M. Tahara, N. Okano, T. Inamura, H. Hosoda, Plastic deformation behaviour of single-crystalline martensite of Ti–Nb shape memory alloy, Sci. Rep. 7 (2017) 15715.
[28] J.J. Gao, I. Thibon, P. Castany, T. Gloriant, Effect of grain size on the recovery strain in a new Ti–20Zr–12Nb–2Sn superelastic alloy, Mater. Sci. Eng. A 793 (2020) 139878.
[29] T. Inamura, J.I. Kim, H.Y. Kim, H. Hosoda, K. Wakashima, S. Miyazaki, Composition dependent crystallography of α"-martensite in Ti–Nb-based β−titanium alloy, Phil. Mag. 87 (2007) 3325–3350.
[30] Y.W. Chai, H.Y. Kim, H. Hosoda, S. Miyazaki, Self-accommodation in Ti–Nb shape memory alloys, Acta Mater. 57 (2009) 4054–4064.
[31] Y.W. Chai, H.Y. Kim, H. Hosoda, S. Miyazaki, Interfacial defects in Ti–Nb shape memory alloys, Acta Mater. 56 (2008) 3088–3097.
[32] E. Bertrand, P. Castany, Y. Yang, E. Menou, T. Gloriant, Deformation twinning in the full-α" martensitic Ti–25Ta–20Nb shape memory alloy, Acta Mater. 105 (2016) 94–103.
[33] J.J. Gao, I. Thibon, D. Laillé, P. Castany, T. Gloriant, Influence of texture and transformation strain on the superelastic performance of a new Ti–20Zr–3Mo–3Sn alloy, Mater. Sci. Eng. A 762 (2019) 138075.
[34] M. Park, W.-T. Chiu, N. Nohira, M. Iwasaki, M. Tahara, H. Hosoda, Microstructure characteristics and superelastic properties of novel Ti–Cr–Sn superelastic alloys, Mater. Sci. Eng. A 869 (2023) 144790.
[35] Y. Zhang, D. Gong, Y. Wang, L.S.R. Kumara, K. Chen, S. Wei, C. Lu, Y. Shen, H. Wang, R. Yang, Y. Hao, Texture-induced anisotropic elastic properties and their temperature dependences in hot-rolled Ti-24Nb-4Zr-8Sn alloy, Mater. Sci. Eng. A 939 (2025) 148493.
[36] J. Gou, G. Liu, T. Yang, X. Liu, Y. Pan, C. Liu, Y. Qian, Y. Liu, Y. Chen, X. Zhang, T. Ma, X. Ren, A high-entropy alloy showing gigapascal superelastic stress and nearly temperature-independent modulus, Nat. Com 16 (2025) 1227.
[37] L. Lilensten, F. Sun, A. Hocini, G. Dirras, P. Vermaut, F. Prima, {332}< 113> mechanical detwinning as a deformation mechanism in the β-metastable Ti-15Mo alloy during cyclic loading, Scripta Mater. 232 (2023) 115503.
[38] E. Bertrand, P. Castany, T. Gloriant, Investigation of the martensitic transformation and the damping behavior of a superelastic Ti–Ta–Nb alloy, Acta Mater. 61 (2013) 511–518.